Earth and Planetary Science Letters 450 (2016) 381–391

Contents lists available at ScienceDirect

Earth and Planetary Science Letters

www.elsevier.com/locate/epsl

The acid and alkalinity budgets of weathering in the Andes–Amazon system: Insights into the erosional control of global biogeochemical cycles

Mark A. Torres[a,b,*], A. Joshua West[a], Kathryn E. Clark[c,d], Guillaume Paris[b], Julien Bouchez[e], Camilo Ponton[a,b], Sarah J. Feakins[a], Valier Galy[f], Jess F. Adkins[b]

[a] *Department of Earth Sciences, University of Southern California, Los Angeles, CA, USA*
[b] *Division of Geological and Planetary Sciences, California Institute of Technology, Pasadena, CA, USA*
[c] *School of Geography and the Environment, University of Oxford, Oxford, UK*
[d] *Department of Earth and Environmental Science, University of Pennsylvania, Philadelphia, PA, USA*
[e] *CNRS – Institut de Physique du Globe de Paris – Université Sorbonne Paris-Cité, Paris, France*
[f] *Department of Marine Chemistry and Geochemistry, Woods Hole Oceanographic Institution, Woods Hole, MA, USA*

ARTICLE INFO

Article history:
Received 25 November 2015
Received in revised form 8 June 2016
Accepted 9 June 2016
Available online 28 June 2016
Editor: D. Vance

Keywords:
chemical weathering
Andes
Amazon
Pyrite
oxidation

ABSTRACT

The correlation between chemical weathering fluxes and denudation rates suggests that tectonic activity can force variations in atmospheric pCO_2 by modulating weathering fluxes. However, the effect of weathering on pCO_2 is not solely determined by the total mass flux. Instead, the effect of weathering on pCO_2 also depends upon the balance between 1) alkalinity generation by carbonate and silicate mineral dissolution and 2) sulfuric acid generation by the oxidation of sulfide minerals. In this study, we explore how the balance between acid and alkalinity generation varies with tectonic uplift to better understand the links between tectonics and the long-term carbon cycle.

To trace weathering reactions across the transition from the Peruvian Andes to the Amazonian foreland basin, we measured a suite of elemental concentrations (Na, K, Ca, Mg, Sr, Si, Li, SO_4, and Cl) and isotopic ratios ($^{87}Sr/^{86}Sr$ and $\delta^{34}S$) on both dissolved and solid phase samples. Using an inverse model, we quantitatively link systematic changes in solute geochemistry with elevation to downstream declines in sulfuric acid weathering as well as the proportion of cations sourced from silicates. With a new carbonate-system framework, we show that weathering in the Andes Mountains is a CO_2 source whereas foreland weathering is a CO_2 sink. These results are consistent with the theoretical expectation that the ratio of sulfide oxidation to silicate weathering increases with increasing erosion. Altogether, our results suggest that the effect of tectonically-enhanced weathering on atmospheric pCO_2 is strongly modulated by sulfide mineral oxidation.

1. Introduction

The interaction between water and rock at the Earth's surface plays an important role in the biogeochemical cycling of carbon, sulfur, and oxygen (Berner, 1989; Lerman et al., 2007; Berner and Berner, 2012). Silicate mineral dissolution by carbonic acid removes carbon from the ocean–atmosphere system by providing the cations and alkalinity necessary for the burial of carbonate minerals (Lerman et al., 2007; Berner and Berner, 2012). At the same time, minerals that are rich in reduced sulfur (e.g., pyrite; FeS_2) react with oxygen to produce sulfuric acid, which can dissolve carbonate minerals and release carbon into the ocean–atmosphere system (Lerman et al., 2007; Calmels et al., 2007; Torres et al., 2014). The effect of weathering on atmospheric CO_2 and O_2 is thus set by the relative contents of silicate, carbonate, and sulfide minerals, and their reactivity at surface conditions (Lerman et al., 2007; Brantley et al., 2013).

While the supply of silicate, carbonate, and sulfide minerals available for weathering depends upon lithology, intrinsic variability in the reaction rates of different minerals can influence their relative importance in weathering budgets. For example, carbonate and sulfide minerals, which are often present as trace constituents of nominally silicate bedrock, can disproportionately affect weathering budgets due to their rapid dissolution kinetics (Hercod et al., 1998; White et al., 1999; Calmels et al., 2007). Thus, the extent

---

[*] Corresponding author at: Division of Geological and Planetary Sciences, California Institute of Technology, Pasadena, CA, USA.
E-mail address: mtorres@caltech.edu (M.A. Torres).

http://dx.doi.org/10.1016/j.epsl.2016.06.012
0012-821X/© 2016 Elsevier B.V. All rights reserved.

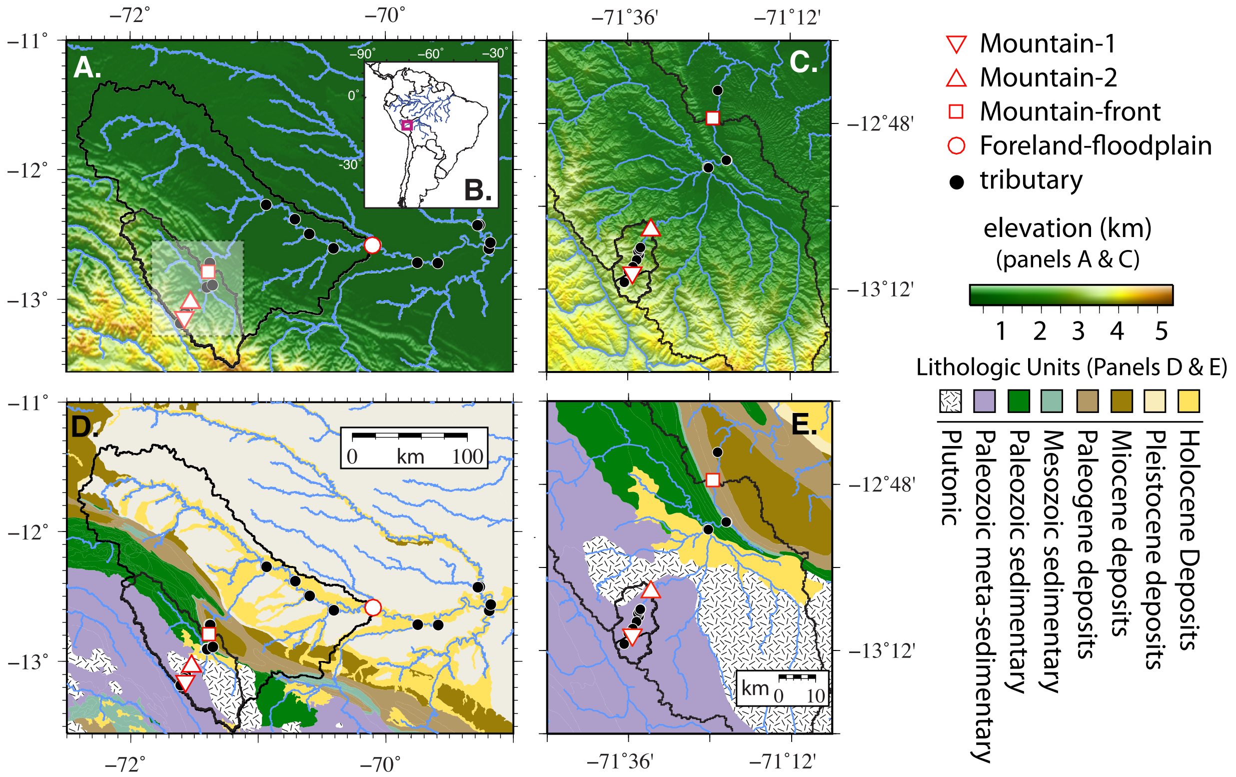

Fig. 1. Study site. (A) Topographic map of the Kosñipata–Madre de Dios study region. The red open symbols indicate the locations of the mainstem sampling sites. Tributaries are shown as black filled circles. Catchment boundaries are shown as black outlines. (B) Inset showing the location of the study region within the larger Amazon system. (C) Topographic map of the Andean portion of the study region (i.e. the area highlighted by the white box in panel A). The locations of the Mountain-1 and Mountain-2 sites are shown as red open base-down and base-up triangles respectively. (D & E) Geological maps of the Kosñipata–Madre de Dios study region (Mendívil Echevarría and Dávila Manrique, 1994; Carlotto Caillaux et al., 1996; Vargas Vilchez and Hipolito Romero, 1998; INGEMMET, 2013). (For interpretation of the references to color in this figure legend, the reader is referred to the web version of this article.)

to which reactive trace phases dominate the weathering budget should be sensitive to erosional and hydrologic processes, which together control the characteristic timescales over which weathering occurs (West, 2012; Maher and Chamberlain, 2014). While available data are consistent with an erosional control on sulfide mineral oxidation fluxes (e.g., Calmels et al., 2007), only a few studies have investigated the effects of changing acid sources (i.e. carbonic vs. sulfuric) on weathering processes across environmental gradients (e.g., Galy and France-Lanord, 1999). Such studies are required for understanding how global biogeochemical cycles respond to changes in erosional and climatic forcings.

In this study, we generate a new data set of solute concentrations and isotopic ratios in order to partition the dissolved load of rivers draining the Andes Mountains and Amazon foreland floodplain in Peru between different mineral (carbonate and silicate) and acid (carbonic and sulfuric) sources. We establish a mixing model incorporating major and trace element ratios, strontium isotopic ratios ($^{87}Sr/^{86}Sr$), and sulfur isotopic ratios measured on both solid and dissolved phase samples. The results of the mixing model are used to determine how the effect of chemical weathering on atmospheric CO_2 varies across the transition from the steep slopes and rapid erosion in the Andes to the foreland floodplain of Peru, a transition that is thought to reflect a gradient in the timescales that minerals undergo weathering (Dosseto et al., 2006; Torres et al., 2015).

2. Methods

2.1. Study site

In this study, we focus on the Madre de Dios River in Peru, its major tributaries, and its headwaters in the Andean Kosñipata valley (Fig. 1). The Madre de Dios River is a major tributary of the Madeira River, which is the second largest Amazonian river in terms of sulfate and bicarbonate fluxes (Gaillardet et al., 1997). The Kosñipata–Madre de Dios system is the focus of an on-going investigation of both the organic (Clark et al., 2013; Ponton et al., 2014; Clark et al., 2016) and inorganic (Torres et al., 2015) carbon cycles, which provides a useful context for this study.

In order to study how weathering processes differ as a function of erosional forcing, we divide the Kosñipata–Madre de Dios study site into three regions based on the elevation of the catchment outlet, following Torres et al. (2015). Our divisions correspond to the high Andes (outlet elevation >1300 m), the Andean mountain front (outlet elevation >400 m), and the foreland-floodplain region (outlet elevation <400 m; Moquet et al., 2011). Like Torres et al. (2015), we focus our attention on a set of nested catchments that span these regions. In this study, we also consider a series of tributary sub-catchments utilized in Ponton et al. (2014).

To constrain weathering processes occurring in the high Andes, we focus on the Kosñipata River sampled at the Wayqecha and San Pedro gauging stations (Fig. 1). The catchment area of the Kosñipata River is predominately underlain by Paleozoic metasedimentary rocks with a minor proportion of felsic plutonic rocks (Fig. 1e). For simplicity, we will refer to the Kosñipata River sampling sites collectively as the Mountain sites, with Mountain-1 referring to the Wayqecha gauging station and Mountain-2 referring to the San Pedro gauging station.

To integrate weathering processes over the entire range of elevations in the Peruvian Andes that contribute to the Amazonian weathering budget, we focus on the Alto Madre de Dios River sampled at the Manu Learning Center (MLC) gauging station, which is at the mountain front (Fig. 1). The catchment area of the

Alto Madre de Dios River is predominately underlain by Paleozoic meta-sedimentary rocks, felsic plutonic rocks, and Paleozoic marine sedimentary rocks (Fig. 1d). We will refer to the Alto Madre de Dios River sampled at the Manu Learning Center (MLC) as the Mountain-front site.

To understand weathering processes in the foreland floodplain region, we focus on the Madre de Dios River sampled at the CICRA-Los Amigos gauging station (Fig. 1). In the foreland floodplain region, the catchment area of the Madre de Dios River is predominately underlain by sediments shed from the Andes with additional contributions from Cretaceous marine sediments and Cenozoic continental deposits (Fig. 1d). We will refer to the Madre de Dios River sampled at the CICRA gauging station as the Foreland-floodplain site.

For our analysis, we focus on time series data from each of the gauging stations (equivalent to samples discussed in Clark et al., 2013, 2014; Torres et al., 2015) and two elevation transects (wet and dry seasons; March & August 2013) that include a variety of tributary samples (see Ponton et al., 2014). In addition to tributaries within each of the four study catchments, the elevation transects include mainstem and tributary samples collected downstream of the Foreland-floodplain site.

Our samples were collected at different times using slightly different methods (see below, Appendix A.1, & Appendix A.2). As each analysis is introduced, the number of samples analyzed is indicated in parentheses. A subset of the solute concentration data used in this study was originally published in Torres et al. (2015). All of the data are included as supplementary material.

2.2. Solid phase geochemical analyses

Samples of river bank sediments and rocks were collected from across the entire study site in order to constrain the elemental and isotopic composition of different lithologic end-members. The details of each analytical method employed are included as supplementary material. Briefly, ground sediment and rock samples were used to measure the concentrations of non-volatile elements using X-ray fluorescence spectroscopy (XRF; $n = 25$), the concentrations of carbonate minerals using infrared spectroscopy on evolved CO_2 ($n = 16$), and the sulfur isotopic composition of reduced sulfur compounds using a gas-source isotope ratio mass spectrometer (ThermoQuest Finnigan Delta PlusXL) after either chromium extraction ($n = 3$; Gröger et al., 2009) or drilling macroscopic veins ($n = 5$). Replicate extractions of rock samples and pyrite standards revealed variability in $\delta^{34}S$ of up to 0.2‰.

Samples of un-ground riverbank sediments were also subjected to a sequential leaching procedure to isolate the chemical composition of the carbonate component (Leleyter and Probst, 1999). The leachates were analyzed by microwave plasma atomic emission spectroscopy (MP-AES; $n = 18$).

2.3. Dissolved phase geochemical analyses

All water samples were filtered using a 0.2 μm porosity membrane filter within 24 h of collection and split into multiple aliquots. One aliquot was preserved by adding concentrated acid. Detailed sampling and analytical methodologies are included as supplementary material (Appendix A.2). Briefly, the acidified samples were analyzed for cation and Si concentrations by MP-AES ($n = 299$), sulfur isotopic composition of sulfate by multicollector inductively coupled plasma mass spectrometry (MC-ICP-MS; $n = 75$; Paris et al., 2013), and $^{87}Sr/^{86}Sr$ of dissolved Sr by MC-ICP-MS ($n = 37$). For sulfur isotopes, replicate purification of river water samples and seawater standards revealed variability in $\delta^{34}S$ of up to 0.2‰. For radiogenic Sr isotopes, replicate purification of river water samples revealed variability in $^{87}Sr/^{86}Sr$ of up to 1×10^{-4}. Un-acidified samples were analyzed for Cl and SO_4 concentrations by ion chromatography ($n = 299$).

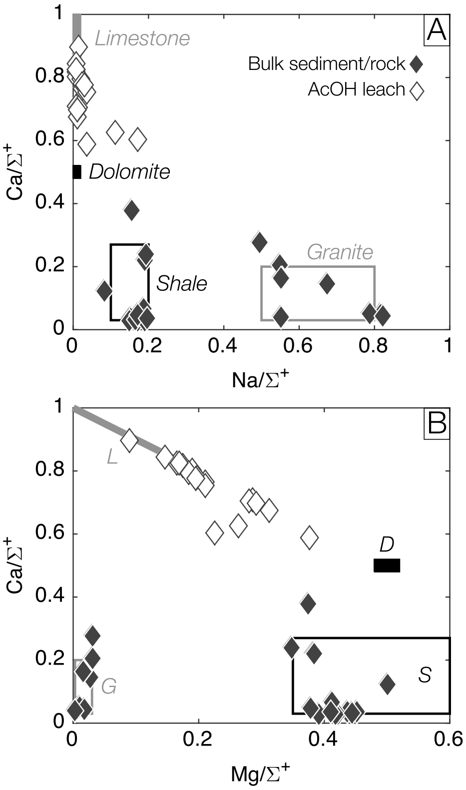

Fig. 2. Solid phase geochemistry. (A) Solid-phase Na/Σ^+ and Ca/Σ^+. (B) Solid-phase Mg/Σ^+ and Ca/Σ^+. Bulk sediment samples are shown as closed diamonds and uncorrected acetic acid leachates are shown as open diamonds. Boxes show the ranges of elemental ratios associated with the lithologic end-members used in the mixing model (L = limestone, D = dolomite, G = granite, S = shale).

3. Results

3.1. Solid phase analyses

The solid-phase samples analyzed in this study are composed of a mixture of minerals and thus provide information regarding the lithologic sources of different solutes. Here, we focus on the results that allow for the chemical composition of the carbonate and silicate phases to be isolated. In the following sections, ratios with the subscript “sediment” refer to the XRF measurements of the bulk sediments. Ratios with the subscript “leach” refer to the analyses of leachates of the bulk sediments. The data will be reported as the ratio of the concentration of an element to the total concentration of all major cations (Σ^+; $Na + K + Ca + Mg$) in units of charge equivalents.

3.1.1. Solid phase major and trace element ratios

Bulk $Na/\Sigma^+_{sediment}$, $Ca/\Sigma^+_{sediment}$, $Mg/\Sigma^+_{sediment}$, and $Sr/\Sigma^+_{sediment}$ range from 0.08 to 0.82 eq/eq, 0.03 to 0.38 eq/eq, 0.002 to 0.50 eq/eq, and 0.9 to 2.3 meq/eq respectively (Fig. 2). Co-variation between $Na/\Sigma^+_{sediment}$ and $Mg/\Sigma^+_{sediment}$ suggests two sample groups: a high $Mg/\Sigma^+_{sediment}$ group and a low $Mg/\Sigma^+_{sediment}$ group (Fig. 2b). Both the high and low $Mg/\Sigma^+_{sediment}$ groups have similar ranges of $Ca/\Sigma^+_{sediment}$ (Fig. 2b).

Measured carbonate concentrations range from 3.5 to 7080 μg carbonate carbon/g sediment. For some samples, carbonate contents are sufficient to account for a significant proportion of the bulk Mg and Ca content. However, the ranges of each ratio are

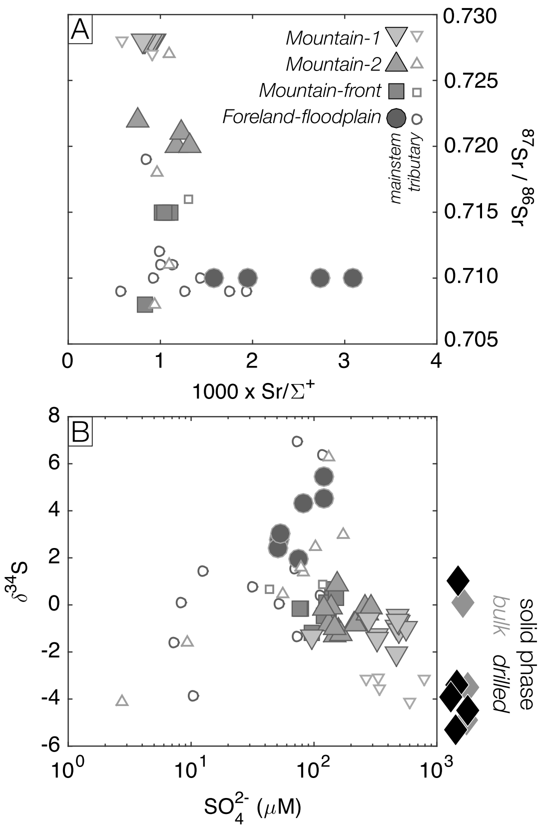

Fig. 3. Dissolved Sr and S isotope geochemistry. In this and all subsequent figures, base-up triangles refer to samples from the Mountain-1 site (Kosñipata River at Wayqecha catchment; lightest gray), base-down triangles refer to samples from the Mountain-2 site (Kosñipata River at San Pedro catchment; light gray), squares refer to samples from the Mountain-front site (Alto Madre de Dios River at MLC catchment; dark gray), and circles refer to samples from the Foreland-floodplain site (Madre de Dios River at CICRA catchment; darkest gray). Larger filled symbols correspond to mainstem samples and smaller open symbols correspond to tributaries. (A) Dissolved radiogenic Sr isotope ratios. (B) Dissolved S isotope ratios. Solid phases S isotope ratios are shown as diamonds to the right of the plot. Gray diamonds refer to bulk chromium-reducible sulfur analyses (Gröger et al., 2009) and black diamonds refer to drilled sulfide mineral veins.

not significantly affected by excluding samples with molar carbonate contents greater than 5% of the combined molar Ca and Mg content, which implies that variations in elemental ratios are not primarily driven by variable carbonate contents (Fig. 2).

All of the analyzed leachates contain Al and Si, which suggests that the leaching procedure affects both carbonate and silicate minerals. For Na/Σ^+_{leach}, a strong correlation with Al concentrations implies that most of the measured Na is sourced from silicate minerals, as expected given the low reported Na/Ca for carbonates (Gaillardet et al., 1997). While Mg/Σ^+_{leach} and Sr/Σ^+_{leach} are also positively correlated with Al concentrations, the variability in these elemental ratios cannot be explained by silicate contributions alone (Fig. 2).

3.1.2. Solid phase reduced inorganic sulfur isotope ratios

The $\delta^{34}S$ of inorganic reduced S phases extracted from three bulk rock samples and five drilled sulfide veins range from −5.3 to +1.0‰ (Fig. 3b). For the three bulk samples, there is no correlation between $\delta^{34}S$ and the reduced S content of the rock, which was measured as the mass of extracted Ag_2S.

3.2. Dissolved phase analyses

For the time series samples taken from the mainstem rivers, changes in solute concentrations with discharge are discussed in Torres et al. (2015). Here, we focus on elemental and isotopic ratios for both the time series and tributary samples (see section 2.1) and consider their implications for weathering reactions. Like the solid phase data, dissolved phase data will be reported as the ratio of the concentration of an element to the total concentration of all cations in units of charge equivalents.

3.2.1. Dissolved phase major and trace element ratios

For the mainstem rivers, both of the Mountain sites as well as the Mountain-front site have very similar ranges of Na/Σ^+ (Fig. 4a). In contrast, the mainstem at the Foreland-floodplain site has lower Na/Σ^+ than the Andean catchments (Fig. 4a). This decrease in Na/Σ^+ at the Foreland-floodplain site is associated with an increase in Ca/Σ^+ (Fig. 4b). Relative to the Mountain-front site, the two Mountain catchments are enriched in Mg (high Mg/Σ^+; Fig. 4b). For all samples, Li/Σ^+ and SO_4/Σ^+ are positively correlated with each other and with Mg/Σ^+ (Fig. 4c–d). Broadly, Sr/Σ^+ of the mainstem is slightly greater at the Foreland-floodplain site relative to the Mountain and Mountain-front sites (Fig. 3a).

3.2.2. Dissolved radiogenic strontium isotope ratios

The $^{87}Sr/^{86}Sr$ of dissolved strontium decreases with decreasing sampling elevation for the mainstem rivers (Fig. 3a). The samples from the Mountain-1 and Mountain-2 sites have $^{87}Sr/^{86}Sr$ that range from 0.727–0.728 and 0.719–0.721 respectively. All of the samples from the Mountain-front site have a similar $^{87}Sr/^{86}Sr$ of 0.715 except for one sample collected in the wet season of 2013 that has a lower value of 0.708. Samples from the Foreland-floodplain site all have a similar $^{87}Sr/^{86}Sr$ of 0.709.

None of the tributaries within the Mountain catchments have $^{87}Sr/^{86}Sr$ that are higher than the mainstem sampled at the Mountain-2 site (Fig. 3a). However, some Mountain tributaries have much lower $^{87}Sr/^{86}Sr$ than the mainstem (Fig. 3a). Tributaries of the Mountain-front site also have low $^{87}Sr/^{86}Sr$ (i.e. 0.708–0.709). Foreland-floodplain tributaries are more variable and have $^{87}Sr/^{86}Sr$ that range from 0.709 to 0.718.

3.2.3. Sulfate-sulfur isotope ratios

Broadly, the $\delta^{34}S$ of dissolved SO_4 ($\delta^{34}S_{sulfate}$) increases with decreasing sampling elevation for the mainstem rivers (Fig. 3b). The $\delta^{34}S_{sulfate}$ in the Mountain-1 and Mountain-2 sites ranges from −2.1 to −0.5‰ and from −1.3 to +0.89‰ respectively. The $\delta^{34}S_{sulfate}$ in the Mountain-front site ranges from −0.5 to +0.7‰. The $\delta^{34}S_{sulfate}$ in the Foreland-floodplain site ranges from +2 to +5.5‰.

Tributaries have highly variable $\delta^{34}S_{sulfate}$ that ranges from −3.8 to +6.9‰ (Fig. 3b). Considering all of the mainstem and tributary samples together shows that samples with either high or low SO_4 concentrations typically have low $\delta^{34}S_{sulfate}$ whereas samples with intermediate SO_4 concentrations have higher $\delta^{34}S_{sulfate}$ (Fig. 3b).

4. Discussion

Assessing the effects of weathering processes on atmospheric CO_2 requires 1) partitioning dissolved cations between silicate and carbonate sources (Gaillardet et al., 1997; Galy and France-Lanord, 1999; Moquet et al., 2011; Spence and Telmer, 2005; Bickle et al., 2015) and 2) partitioning the acid budget between weathering by carbonic and sulfuric acids (Hercod et al., 1998; Galy and France-Lanord, 1999; Spence and Telmer, 2005; Calmels et al., 2007; Das et al., 2012; Torres et al., 2014). With these goals in mind, we first qualitatively compare the dissolved- and solid-phase measurements to identify key lithologic end-members for both cations (section 4.1) and sulfate (section 4.2). Next, we develop a quantitative mixing model that jointly apportions cation and sulfate sources (section 4.3). After we evaluate the mixing

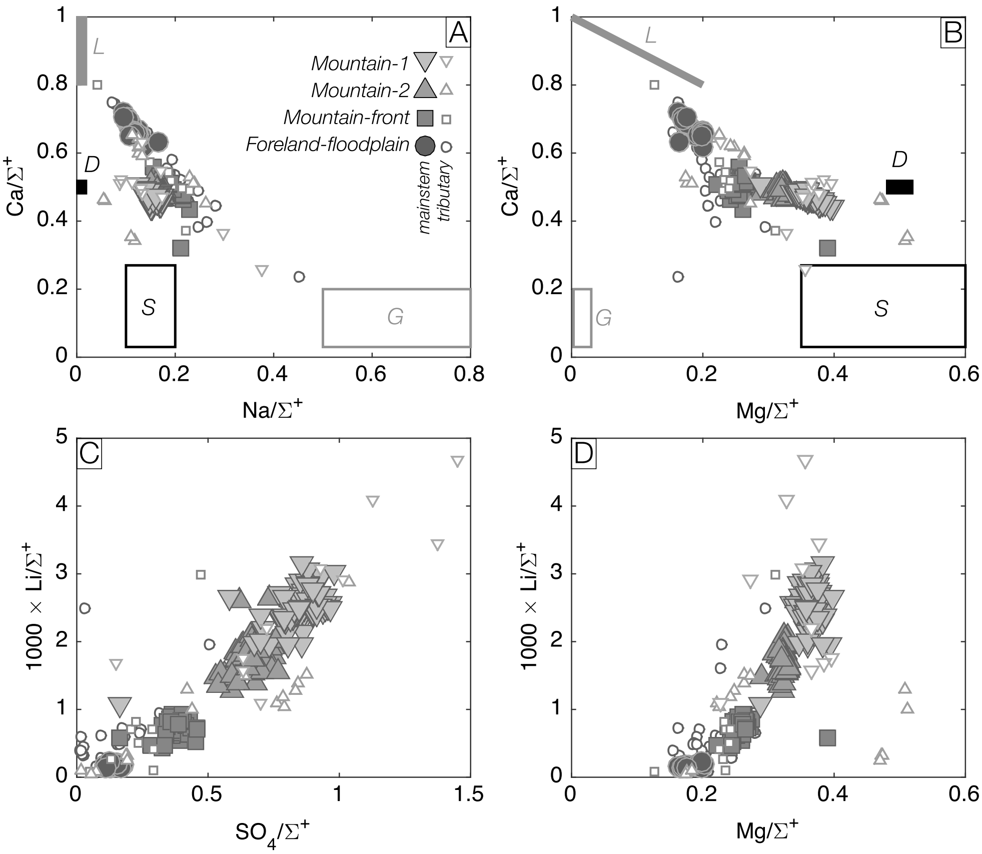

Fig. 4. Dissolved phase geochemistry. (A) Na/Σ^+ and Ca/Σ^+, (B) Mg/Σ^+ and Ca/Σ^+, (C) SO_4/Σ^+ and Li/Σ^+, and (D) Mg/Σ^+ and Li/Σ^+ of the dissolved phase samples. Boxes show the ranges of elemental ratios associated with the lithologic end-members used in the mixing model (L = limestone, D = dolomite, G = granite, S = shale).

model (section 4.4), we develop a new interpretative framework that uses the mixing model results to identify the effects of weathering on atmospheric CO_2 (section 4.5). We conclude our discussion by linking the observed effects of weathering on atmospheric CO_2 with their environmental drivers (section 4.6).

4.1. Lithologic source partitioning – general considerations

Scatter plots comparing different solute concentration ratios show varying degrees of dispersion (Fig. 4), which is consistent with mixing between more than two end-members. The elemental ratios associated with the solid phase measurements bracket all of the dissolved phase measurements (Fig. 4), which implies that the solid phase measurements are viable as lithologic end-members and non-stoichiometric or secondary processes are not absolutely required to explain the concentration ratios of the major solutes (cf. Bickle et al., 2015). We note that this is also true for other elemental ratios (e.g., sodium to calcium ratios).

Since the bulk solid phase measurements indicate the presence of a Mg-rich and a Mg-poor silicate component, we define two silicate end-members: "shale" (Mg-rich) and "granite" (Mg-poor). Note that by shale and granite, we are referring specifically to the silicate component of these lithologies. These identifications are consistent with geologic maps that show the presence of both marine (meta)sedimentary rocks and igneous intrusions within the study area (Fig. 1c, e). Similarly, we define Mg-rich and Mg-poor carbonate end-members (dolomite and limestone respectively; Fig. 2). The elemental ratios selected for each end-member encompass the range of solid phase measurements (Fig. 2). We include a wider range of Mg/Σ^+ for the shale end-member to reflect the preferential weathering of Mg-rich sheet silicates (Fig. 2b), which is not required by the data but is formally possible. Exact end-member definitions are provided in Table 1.

The low dissolved Na/Σ^+ and Mg/Σ^+ ratios observed for some tributaries and the mainstem at the Foreland-floodplain site are consistent with a greater contribution from the dissolution of limestone relative to the upstream sites (the Mountain and Mountain-front sites). These sites also have low $^{87}Sr/^{86}Sr$ (0.708 to 0.709), which is consistent with limestone dissolution (Andean Limestone $^{87}Sr/^{86}Sr = 0.707$ to 0.708; Gaillardet et al., 1997).

The Mountain and Mountain-front sites are enriched in Na relative to the Foreland-floodplain site, which implies a greater contribution from either of the silicate end-members (Fig. 4a). The Mountain sites along with many of their tributaries appear to be enriched in Mg relative to the Mountain-front site (Fig. 4b). This Mg enrichment could be due to either shale or dolomite weathering. Co-variation between Mg/Σ^+ and Li/Σ^+ (Fig. 4c–d) suggests at least some contribution from shale weathering because shales are enriched in lithium and carbonates are not (Dellinger et al., 2015). Moreover, the high values of $^{87}Sr/^{86}Sr$ at the Mountain sites (0.720–0.728) are similar to those reported for Andean shales (0.728–0.750; Roddaz et al., 2005; Dellinger et al., 2015; Fig. 3a). However, the high values of Ca/Σ^+ for the Mountain catchments require some contribution from carbonate weathering based on the low Ca/Σ^+ of silicate sources (Figs. 2 and 4a, b).

In summary, the major and trace element ratios suggest that cations are sourced predominately from carbonate and silicate mineral dissolution. This is consistent with the observation that more than 90% of our samples have Cl concentrations lower than 20 μM, which is the maximum concentration of atmospherically sourced Cl proposed by Gaillardet et al. (1997) for the Andes/Amazon system. The samples that do exceed 20 μM Cl do not exceed 60 μM Cl. Rivers in the Andes/Amazon system with known evapor-

Table 1
End-members used in mixing model.

Shale	Range sampled	Notes	Citation	Dolomite	Range sampled	Notes	Citation
Na/Σ^+	0.1 to 0.2			Na/Σ^+	0		
Ca/Σ^+	0.03 to 0.3			Ca/Σ^+	0.5		
Mg/Σ^+	0.45 to 0.6	higher than measured to simulate preferential mica weathering		Mg/Σ^+	0.5		
Cl/Σ^+	0			Cl/Σ^+	0		
SO_4/Σ^+	0 to 1	allowed to be > 1 for samples with $SO_4/\Sigma^+ > 1$		SO_4/Σ^+	0 to 1	allowed to be > 1 for samples with $SO_4/\Sigma^+ > 1$	
$\delta^{34}S$	−5 to +1 permil			$\delta^{34}S$	−5 to +1 permil		
Sr/Σ^+	0.0005 to 0.0025			Sr/Σ^+	0.001 to 0.009		
$^{87}Sr/^{86}Sr$	0.728–0.750		1, 2	$^{87}Sr/^{86}Sr$	0.707 to 0.710		2, 4
Li/Na	0.041		2	Li/Na	0		2

Granite	Range sampled	Notes	Citation	Rainfall	Range sampled	Notes	Citation
Na/Σ^+	0.5 to 0.8			Na/Σ^+	0.05 to 0.43	Co-varies with Cl/Σ^+	5
Ca/Σ^+	0.03 to 0.4			Ca/Σ^+	0.2 to 0.65		5
Mg/Σ^+	0.003 to 0.03			Mg/Σ^+	0.1 to 0.2		5
Cl/Σ^+	0			Cl/Σ^+	0.06 to 0.5		5
SO_4/Σ^+	0 to 1	allowed to be > 1 for samples with $SO_4/\Sigma^+ > 1$		SO_4/Σ^+	0.06 to 0.4		5
$\delta^{34}S$	−5 to +1 permil			$\delta^{34}S$	−5 to +9 permil		7
Sr/Σ^+	0.0005 to 0.0025			Sr/Σ^+	0.00005 to 0.005		5
$^{87}Sr/^{86}Sr$	0.704 to 0.720	range increased to match San Pedro River, which drains only granites	3	$^{87}Sr/^{86}Sr$	0.708 to 0.709		4
Li/Na	0.005		2	Li/Na	0		

Limestone	Range sampled	Notes	Citation	Evaporite	Range sampled	Notes	Citation
Na/Σ^+	0			Na/Σ^+	0 to 0.1		
Ca/Σ^+	0.8 to 1			Ca/Σ^+	0.85 to 0.9		
Mg/Σ^+	0 to 0.2	Co-varies with Ca/Σ^+		Mg/Σ^+	0 to 0.15		6
Cl/Σ^+	0			Cl/Σ^+	0 to 0.1	Co-varies with Na/Σ^+	
SO_4/Σ^+	0 to 1	allowed to be > 1 for samples with $SO_4/\Sigma^+ > 1$		SO_4/Σ^+	0.85 to 0.9	Co-varies with Ca/Σ^+	
$\delta^{34}S$	−5 to +1 permil			$\delta^{34}S$	+10 to +19 permil		7, 8, 9
Sr/Σ^+	0.001 to 0.009			Sr/Σ^+	N/A		
$^{87}Sr/^{86}Sr$	0.707 to 0.710		2, 4	$^{87}Sr/^{86}Sr$	N/A		
Li/Na	0			Li/Na	N/A		

For all end members, $((Mg/\Sigma^+) + (Na/\Sigma^+) + (Ca/\Sigma^+))$ cannot exceed 1.
[1] Roddaz et al., 2005; [2] Dellinger et al., 2015; [3] Petford and Atherton, 1996; [4] Gaillardet et al., 1997; [5] Torres et al., 2015; [6] Lerman et al., 2007; [7] Longinelli and Edmond, 1983; [8] Paytan et al., 1998; [9] Louterbach et al., 2014.

ite contributions typically have much higher Cl concentrations (e.g., the Huallaga River with 848 ± 421 μM Cl; Moquet et al., 2011).

A significant contribution from sulfate evaporites is unlikely for our sites due to the consistent and overall high Mg/Σ^+ and Sr/Σ^+ ratios observed, as sulfate salts such as gypsum ($CaSO_4 \cdot 2H_2O$) typically have very low Mg/Ca and Sr/Ca ratios (< 1 mmol/mol; Lu et al., 1997; Playà and Rosell, 2005; Lerman et al., 2007). Put another way, solute concentration ratios place a strong constraint on the maximum contribution of sulfate evaporites. This can be explored more rigorously by incorporating information about sulfate sources from sulfur isotopes.

4.2. Sulfate sources

In order to quantify the proportion of weathering driven by sulfuric acid, it is necessary to account for all possible sources of sulfate in order to avoid an overestimation of the amount of sulfide mineral oxidation. The main environmental sources of sulfate include sulfide mineral oxidation, atmospheric deposition, and the dissolution of sulfate evaporites. Here, we review sulfur isotopic constraints on each of these end-members that can be combined with solute concentration ratios (section 4.1) to jointly infer cation and sulfate sources (section 4.3). Additionally, we discuss the potential for sulfur isotope fractionation, which, if significant, could lead us to underestimate the role of sulfide mineral oxidation.

Since the oxidative dissolution of sulfide minerals should not be accompanied by significant sulfur isotope fractionation (Balci et al., 2007), our solid-phase measurements of $\delta^{34}S$ can be used to predict the $\delta^{34}S$ of rivers where the sulfate budget is dominated by sulfide mineral oxidation (Fig. 3b). The overlap between $\delta^{34}S$ of dissolved sulfate from the mainstem at both of the Mountain sites and the measured $\delta^{34}S$ of rock samples suggests that sulfide mineral oxidation dominates at these sites (Fig. 3b).

Rainwaters often have SO_4/Cl ratios greater than seawater, which suggests that SO_4 is added to precipitation as a result of anthropogenic or biological processes (Andreae et al., 1990). These additional sources are generally characterized by low $\delta^{34}S$ values, so the $\delta^{34}S$ of atmospheric deposition should be lower than seawater (+21‰; Paris et al., 2013). Two measurements of Amazonian rainwater taken from Brazil and Colombia have $\delta^{34}S$ values of +10 to +11‰, confirming that SO_4 in Amazonian precipitation reflects a mixture between biogenic and seawater aerosols (Longinelli and Edmond, 1983). The pure foreland floodplain tributaries within our study area (e.g., the Los Amigos and Chiribi Rivers), which are likely to derive most of their SO_4 from atmospheric deposition, have very low SO_4 concentrations (i.e. $\leq$10 μM) and low $\delta^{34}S$ values (i.e. $<$0‰). The difference in $\delta^{34}S$ values between foreland-floodplain tributaries and previous rainwater measurements (Longinelli and Edmond, 1983) could result from the observed spatial variability in the deposition of seawater aerosols (Stallard and Edmond, 1981).

Sulfate evaporite minerals of marine origin are expected to have high $\delta^{34}S$ values. For example, Paleozoic marine evaporites in the Andes have $\delta^{34}S$ near $+10‰$ (Longinelli and Edmond, 1983). Similarly, Paleocene-aged gypsum deposits in the reported in the foreland-floodplain region by Louterbach et al. (2014) likely have $\delta^{34}S$ up to $+19‰$ (Paytan et al., 1998). Potentially, a small evaporite contribution could explain the high $\delta^{34}S$ observed in some river samples (up to $+6‰$). However, the magnitude of any evaporite contribution will ultimately be limited by solute concentration ratios (see section 4.1).

Besides a small evaporite contribution, high $\delta^{34}S$ of dissolved sulfate could be caused by sulfur isotopic fractionation induced by microbial sulfate reduction (Detmers et al., 2001; Yi-Balan et al., 2014). Sulfate reduction is consistent with the observation that sulfate concentrations decrease with increasing $\delta^{34}S$ values for the samples with high to intermediate sulfate concentrations (Fig. 3b). However, in order for reduction to affect the $\delta^{34}S$ of sulfate, the product, H_2S, has to be exported from the catchment without being re-oxidized if the supply of sulfur from bedrock erosion is approximately equal to the export flux of sulfur (Bouchez et al., 2013). While it is not known if such a steady-state assumption is valid for this and other modern river systems, it remains a useful "null" hypothesis.

While gaseous H_2S is measurable in the atmosphere above the Amazon, modeled export fluxes of H_2S are small relative to riverine fluxes of sulfate (Andreae et al., 1990 and see below). To explain a similar trend in the $\delta^{34}S$ of Himalayan rivers, Turchyn et al. (2013) proposed that some H_2S is precipitated as secondary sulfide minerals. Assuming that the S cycle within the catchments of Turchyn et al. (2013) is at steady-state, this mechanism requires that secondary sulfides are eroded without being re-oxidized. Alternative mechanisms, such as the loss of sulfur intermediates during oxidation (Hindshaw et al., 2016) or the incorporation of reduced sulfur into organic phases, also require the export of reduced sulfur to express sulfur isotope fractionation if the systems are at steady-state with respect to the fluxes of S and S isotopes.

Regardless of the exact mechanism, the mass of reduced S that needs to be exported in order to maintain a steady-state isotopic offset between dissolved sulfate and primary sulfur minerals is dependent upon the fractionation factor. Using the formulation of Bouchez et al. (2013), the isotopic offset of the river relative to primary minerals ($\Delta\delta^{34}S_{River\text{-}Rock}$) can be expressed as:

$$\Delta\delta^{34}S_{River\text{-}Rock} = -\Delta_{sec\text{-}sulf} \times F_c \qquad (1)$$

where $\Delta_{sec\text{-}sulf}$ is the apparent fractionation factor, and F_c is the fraction of the total sulfur flux that is exported as a reduced phase. Based on the sulfate concentration-runoff relationship of Torres et al. (2015) and the runoff time-series of Clark et al. (2014), the annual flux of sulfate from the Mountain-2 site is on the order of 10^3 tons/yr. A similar approach, reported in Clark (2014), yields a suspended sediment flux on the order of 10^5 tons of sediment/yr. Thus, if $\Delta_{sec\text{-}sulf}$ is $-10‰$, each $1‰$ of isotopic offset between dissolved sulfate and primary sulfide minerals requires eroded sediments to contain, on average, 0.1 wt% reduced S. Since some rivers may be enriched by up to 5 to $10‰$ relative to bedrock (Fig. 3b), a larger export flux of reduced sulfur may be required; the trade-offs between fractionation factor, isotopic offset, and amount of reduced sulfur that must be exported are illustrated in Fig. 5. These model predictions could be tested in future work on sulfur cycling in this and other mountainous catchments.

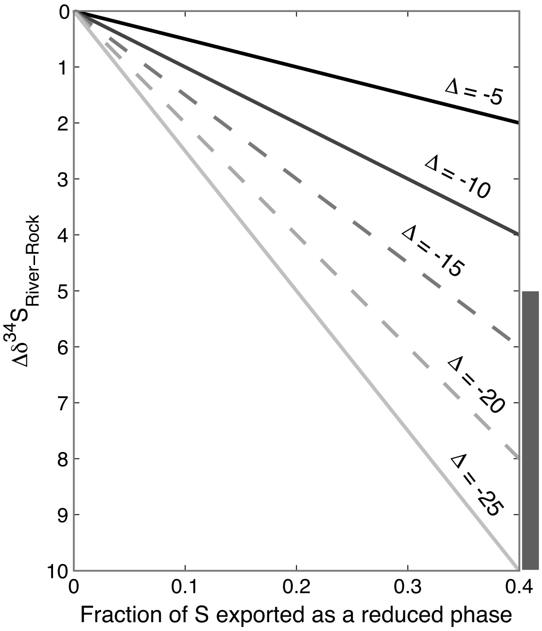

Fig. 5. S isotope fractionation at geomorphic steady state. Variations in the maximum isotopic offset of dissolved sulfate relative to a rock source at geomorphic steady state for different values of the isotopic fractionation factor ($\Delta_{sec\text{-}sulf}$) and the fraction of S exported as a reduced phase calculated using the model of Bouchez et al. (2013). The dashed lines refer to the S isotope fractionation factors utilized by Turchyn et al. (2013) to model S isotope data from rivers in the Himalayan system. The gray rectangle to the right of the plot corresponds to the largest difference between dissolved and solid phase $\delta^{34}S$ measurements observed in this sample set. The range shown is based on either including or excluding the two highest solid phase $\delta^{34}S$ measurements.

4.3. Lithologic source partitioning – quantitative

Based on the preceding discussion (sections 4.1 and 4.2), it is clear that a mixing model needs to account for solutes from limestone, dolomite, shale, granite, and atmospheric deposition. It is somewhat unclear as to whether or not evaporites need to be considered, since the observed variation in $\delta^{34}S$ can be attributed to either a trace evaporite contribution or isotopic fractionation (section 4.2). Ignoring sulfate evaporites could lead to an over-estimation of sulfide mineral oxidation where as ignoring sulfate reduction could lead to an under-estimation. Seeking to be as conservative as possible, we start with a model that considers evaporite minerals as a potential solute source in order to determine whether or not it would significantly affect our results.

In order to partition solutes between different sources, we invert a mixing model based on a subset of the measured elemental and isotopic ratios (Cl/Σ^+, Na/Σ^+, Mg/Σ^+, Ca/Σ^+, SO_4/Σ^+, and $\delta^{34}S$). Details of how we parameterize the model, its assumptions, and how we perform the calculations and uncertainty propagation are described in detail in Appendix A.3. Briefly, the model uses a Monte-Carlo sampling approach to account for uncertainty in the composition of each end-member. For carbonate and silicate sources, the *a priori* range we select for each end-member is equivalent to the ranges shown in Figs. 2, 4, and Table 1. The model assumes that the fractional contributions from each end-member must all be ≥ 0 and sum to one.

In order to incorporate SO_4/Σ^+ and $\delta^{34}S$ into the mixing model, it is necessary to assign values to the carbonate and silicate end-members. For these end-members, SO_4/Σ^+ is directly equal to the proportion of weathering driven by sulfuric acid, which is an unknown we constrain as part of the inversion. For sulfur isotopes, we randomly sample a uniform distribution with the range of measured sulfide mineral $\delta^{34}S$ for carbonate and silicate weathering by sulfuric acid. For the other sulfate sources (rainfall and evaporites), we use uniform distributions with ranges in $\delta^{34}S$ equal to those discussed in section 4.2. The range of sampled SO_4/Σ^+ for rainfall and evaporites are based on direct measurements (Torres et al., 2015) and the stoichiometry of gypsum mixed with trace halite ($Cl/\Sigma^+ = 0$ to 0.1) respectively (Lerman et al., 2007). The exact ranges of end-member values are shown in Table 1.

Using the specified end-member compositions (Table 1), the mixing model can explain the observed geochemical variation for all of the river samples. For a given sample, each random combination of end-member ratios, or simulation, predicts different values for the relative contribution of each end-member. In the following section, we explore how these model predictions co-vary. By adding independent constraints from tracers that were not included in the original model (e.g., Sr and Li), we further constrain the model predictions.

4.4. Mixing model evaluation

4.4.1. Evaporite contributions

For all samples, the predicted contribution of evaporites to the total cation budget is small (max contribution <15%), which is consistent with our qualitative inferences (section 4.1). For all simulations from a single sample, estimates of the evaporite contribution are not correlated with the apportionment of cations between carbonate and silicate sources. Consequently, uncertainties in apportioning the dissolved sulfate budget will not influence the estimated ratio of carbonate to silicate weathering.

In contrast, we observe a negative correlation between the evaporite contribution and the proportion of weathering driven by sulfuric acid for each sample. This outcome is expected since evaporites contribute to the sulfate budget. The variation in the proportion of sulfuric acid weathering is minor for the predicted range of evaporite contributions. As shown in Fig. 6a, the predicted proportion of sulfuric acid weathering is nearly equal to the SO_4/Σ^+ of each sample, as expected if the majority of sulfate was sourced from sulfide mineral oxidation.

While we cannot confidently determine whether or not evaporites drive the observed $\delta^{34}S$ variability (Fig. 3b), the results of our mixing model suggest that ignoring evaporites as a source does not significantly affect our conclusions about either the proportion of carbonate weathering or the proportion of sulfuric acid weathering (Fig. 6a). This is because evaporites have extreme $\delta^{34}S$ values relative to sulfide minerals in this system, so only a small evaporite contribution is necessary to significantly shift $\delta^{34}S$. We can therefore use the SO_4/Σ^+ of each sample directly to infer the proportion of sulfuric acid weathering (Fig. 6a), ignoring evaporite sources and removing $\delta^{34}S$ as a model constraint. This approach allows us to apply our model to all samples and not just the subset of samples with $\delta^{34}S$ measurements.

4.4.2. Carbonate versus silicate weathering

For each sample, the mixing model predicts a wide range of values for the proportion of cation sourced from carbonate weathering (e.g., 30 to 80% of cations from carbonates for Mountain-1). Generally, this range is the greatest for samples from the Mountain catchments and results from uncertainties in partitioning dissolved Mg between shale and dolomite sources. To better constrain estimates of the proportion of carbonate weathering, we can use $^{87}Sr/^{86}Sr$ and Li, which, in theory, should be sensitive to the proportion of shale weathering (F_{shale}) in this system.

Available data suggests that shales within the study area have high $^{87}Sr/^{86}Sr$ relative to granitic rocks and carbonates (Petford and Atherton, 1996; Gaillardet et al., 1997; Roddaz et al., 2005; Dellinger et al., 2015). As a result, riverine $^{87}Sr/^{86}Sr$ can be used to infer F_{shale}. However, high-temperature alteration can produce carbonates with $^{87}Sr/^{86}Sr$ similar to silicate phases (Palmer and Edmond, 1992; White et al., 1999; Jacobson and Blum, 2000). Since the study area contains metamorphosed sedimentary rocks, it is possible that some carbonates have elevated $^{87}Sr/^{86}Sr$. If present but not included within a $^{87}Sr/^{86}Sr$ mixing model, such carbonates would lead to an over-estimation of F_{shale}.

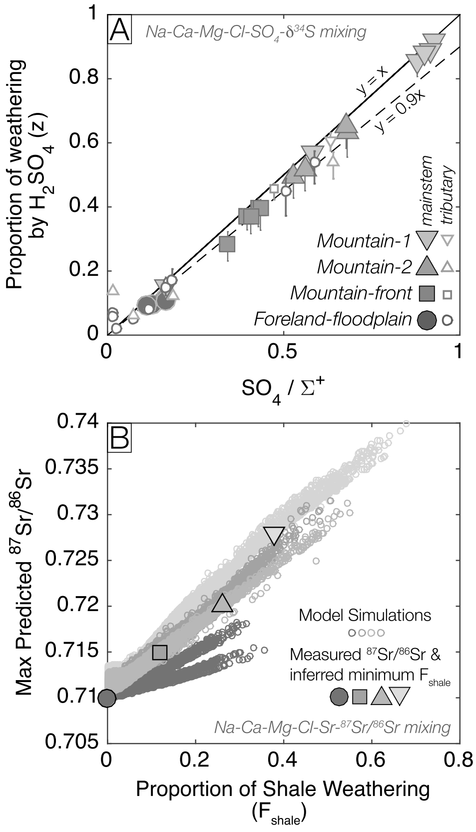

Fig. 6. Mixing model evaluation. (A) Comparison between the measured SO_4/Σ^+ and the predicted proportion of sulfuric acid weathering based on inversion of Cl, Na, Ca, Mg, SO_4, and $\delta^{34}S$ data (symbols depict the median value along with 90% confidence interval). (B) The small open circles show the maximum predicted $^{87}Sr/^{86}Sr$ for simulations with varying proportions of shale weathering (inversion of Cl, Na, Ca, and Mg data). Solid points correspond to the measured $^{87}Sr/^{86}Sr$ and inferred minimum F_{shale} based on a second order polynomial fit. For each sampling locality, the model results are based on all of the individual samples measured for strontium isotope ratios.

Lithium is enriched in shales relative to other silicate lithologies and is practically absent in carbonates (Dellinger et al., 2015). Consequently, Li/Σ^+ can also be used to infer F_{shale}. However, lithium isotopes reveal that lithium does not behave conservatively in Amazonian rivers (Dellinger et al., 2015). Consequently, Li/Σ^+ is likely to under-estimate F_{shale} due to the formation of lithium-bearing clays.

Since $^{87}Sr/^{86}Sr$ may overestimate F_{shale} and Li/Σ^+ may underestimate it, checking for consistency between the two tracers is a useful test. Here, we adopt a forward modeling approach to utilize both $^{87}Sr/^{86}Sr$ and Li/Σ^+ as additional constraints (full description in the supplementary materials). We predict $^{87}Sr/^{86}Sr$ and Li/Σ^+ by combining our model estimates of the fractional contribution from each end-member with constraints on the Sr/Σ^+, Li/Σ^+, and $^{87}Sr/^{86}Sr$ of each end-member from measurements and literature data (Table 1; Roddaz et al., 2005; Petford and Atherton, 1996; Gaillardet et al., 1997; Dellinger et al., 2015). This allows us to view how the predicted $^{87}Sr/^{86}Sr$ and Li/Σ^+ vary as a function of the fractional contribution from each end-member. By comparing these relationships with the measured values, we can identify the subset of model results that best agree with all of the measured tracers.

Under the assumption that all carbonates have low $^{87}Sr/^{86}Sr$, our mixing model produces a strong correlation between $^{87}Sr/^{86}Sr$ and the proportion of shale weathering (F_{shale}). Due to uncertainties in the Sr/Σ^+ and $^{87}Sr/^{86}Sr$ of each end-member, every value of F_{shale} that can describe a single sample is associated with a range of predicted $^{87}Sr/^{86}Sr$. Here, we focus on the maximum $^{87}Sr/^{86}Sr$ value that can be predicted by a value of F_{shale} in order to get an estimate of the minimum F_{shale} needed for major elements and $^{87}Sr/^{86}Sr$ to agree (Fig. 6b).

For the mainstem rivers, we observed a monotonic decrease in $^{87}Sr/^{86}Sr$ with elevation (Fig. 3a). Based on our Sr model analysis, this decrease in $^{87}Sr/^{86}Sr$ implies a decrease in the minimum F_{shale} required for model-data agreement (Fig. 6b). For the Mountain sites, at least 40% (Mountain-1) and 25% (Mountain-2) of cations must be sourced from shale weathering in order to match measured $^{87}Sr/^{86}Sr$ (Fig. 6b). For the Mountain-front and Foreland-floodplain sites, much smaller values of F_{shale} are required ($<$12%; Fig. 6b). An analogous approach applied to Li/Σ^+ suggests minimum F_{shale} values of 25%, 10%, 0%, and 0% for the Mountain-1, Mountain-2, Mountain-front, and Foreland-floodplain sites respectively.

While the minimum values of F_{shale} predicted by Li/Σ^+ are lower than those predicted by $^{87}Sr/^{86}Sr$ (Fig. 6b), both tracers suggest that shale contributions decrease from the Mountain to the Foreland-floodplain sites. Based on the observations that 1) lithium uptake into clays is known to impact Andean rivers (Dellinger et al., 2015), 2) there are no reports of carbonates with high $^{87}Sr/^{86}Sr$ in the study area, and 3) both $^{87}Sr/^{86}Sr$ and Li mixing models predict the same trend in F_{shale} with elevation (Fig. 6b), we will apply the following constraints to our mixing model in order to estimate the proportion of carbonate weathering. At the Mountain-1, Mountain-2, and Mountain-front sites, we will adopt the constraints from $^{87}Sr/^{86}Sr$ and consider only the subset of mixing model results where F_{shale} is greater than 40%, 25%, and 11% respectively. At the Foreland-floodplain site, we will consider the full range of model values. In Fig. 7, we show the 95% confidence interval of the model results that meet the above criteria for each mainstem river.

4.5. *Effects of sulfide mineral oxidation on atmospheric pCO_2*

4.5.1. *Interpretive framework*

Elemental and isotopic ratios allow us to determine the proportions of carbonate weathering and weathering by sulfuric acid in each of the study catchments (Section 4.4). Here we present a framework for understanding the implications of these results for atmospheric pCO_2. Due to gas exchange, the pCO_2 of the atmosphere depends on the pCO_2 of the ocean. To first order, the pCO_2 of the ocean is negatively correlated with the ratio of alkalinity to dissolved inorganic carbon (DIC; Zeebe and Wolf-Gladrow, 2001). Since rivers transport alkalinity and DIC generated by weathering to the ocean, chemical weathering modulates atmospheric pCO_2 through its effect on the marine carbonate system. In Appendix A.5, we show how the proportions of carbonate weathering and weathering by sulfuric acid can be uniquely related to the ratio of alkalinity to DIC generated by weathering and used to predict the effect of weathering on atmospheric pCO_2.

The link between the ratio of alkalinity to DIC generated by weathering and atmospheric CO_2 depends upon the timescale of interest. For example, in the modern ocean, the alkalinity to DIC ratio is ∼1. So, on timescales shorter than that of carbonate burial (10^5–10^6 yrs; Berner and Berner, 2012), atmospheric pCO_2 will increase if rivers supply alkalinity and DIC to the ocean in a ratio that is less than 1. We note that this is strictly valid for modern conditions (i.e. oceanic alkalinity/DIC ≈1). In Fig. 7, the dark gray line shows the proportions of carbonate weathering and weathering driven by sulfuric acid that lead to an alkalinity to DIC ratio of 1. Parameter combinations that plot above this reference line are associated with CO_2 release on timescales shorter than that of carbonate burial for modern conditions.

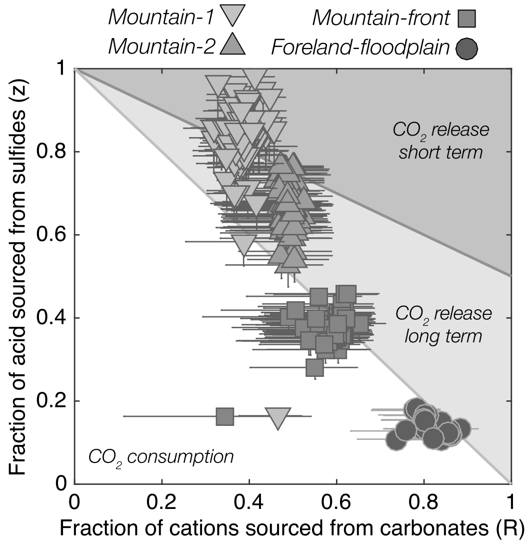

Fig. 7. Effect of weathering on atmospheric pCO_2 in the Kosñipata / Madre de Dios River system. The figure shows the calculated proportions of carbonate weathering (median and 95% confidence interval) and proportions of weathering driven by sulfide mineral oxidation (90 to 100% of measured SO_4/Σ^+; Fig. 6a) for the mainstem sites. The dark gray region defines parameter combinations associated with CO_2 release on short timescales (alkalinity/DIC <1). The light gray region defines parameter combinations associated with CO_2 release on long timescales (alkalinity/DIC <2). The white region defines parameter combinations associated with CO_2 consumption (alkalinity/DIC >2).

Carbonate burial removes alkalinity and DIC from the ocean in a 2 to 1 ratio. So, on timescales longer than carbonate burial but shorter than pyrite burial ($< 10^7$ yrs; Berner and Berner, 2012), atmospheric pCO_2 will increase if rivers deliver alkalinity and DIC to the ocean in a ratio that is less than 2. Consideration of the long-term effects of weathering on pCO_2 in this way is comparable to previous approaches (e.g., Calmels et al., 2007; Torres et al., 2014) and does not necessarily depend on oceanic alkalinity to DIC ratios. In Fig. 7, the proportions of carbonate weathering and weathering driven by sulfuric acid that lead to an alkalinity to DIC ratio of 2 are shown as a light gray line. Parameter combinations that plot above this reference line are associated with CO_2 release on timescales longer than carbonate burial but shorter than pyrite burial. Values below this line are associated with CO_2 consumption (i.e. alkalinity/DIC >2).

4.5.2. *Field data*

Mainstem samples from the Foreland-floodplain site have high proportions of carbonate weathering and low proportions of sulfuric acid weathering (Fig. 7). As a result, weathering in the Foreland-floodplain is characterized by CO_2 consumption (Fig. 7). At the Mountain-front site, mainstem samples have lower proportions of carbonate weathering and higher proportions of sulfuric acid weathering relative to the Foreland-floodplain site (Fig. 7). Mountain-front weathering has no long-term effect on pCO_2 since it generates alkalinity and DIC in a nearly 2 to 1 ratio, which is the same as the ratio associated with carbonate burial (Fig. 7).

Samples of the mainstem river in the Mountain-1 and Mountain-2 sites have lower proportions of carbonate weathering and higher proportions of sulfuric acid weathering (Fig. 7). Because of this combination, weathering in the Mountain sites drives CO_2 release into the atmosphere (Fig. 7). The proportion of sulfuric acid weathering in the Mountain-1 site is sufficiently high for CO_2 to be released on short timescales (alkalinity/DIC <1; Fig. 7). This is consistent with the fact that some of the Mountain-1 tributaries have SO_4 concentrations in excess of total cation concentrations (in charge equivalents; Fig. 4c), which requires that sulfide mineral oxidation outpaces weathering reactions and acidifies the river (analogous to acid mine drainage).

4.6. *An erosional control on the acid budget of chemical weathering*

Based on the data from each of the four mainstem site, we find that the proportion of weathering driven by sulfuric acid increases with increasing elevation (Fig. 7). As a result, mountain weathering is a net CO_2 source and foreland weathering is a net CO_2 sink in the Kosñipata–Madre de Dios system (Fig. 7). We hypothesize that observed differences in the effect of weathering on atmospheric pCO_2 are due to differences in the duration of weathering, which is much longer for material in the foreland relative to the Andes (Dosseto et al., 2006). Since erosion is thought to modulate the residence time of material in the weathering zone (West, 2012; Maher and Chamberlain, 2014), we expect an erosional control on the relationship between weathering and pCO_2.

Generally, rocks contain higher concentrations of silicates than sulfides. Consequently, congruent weathering would not be expected to lead to CO_2 release. Instead, CO_2 release requires some mechanism to preferentially react sulfide minerals relative to silicates. For silicate weathering, models (e.g., West, 2012) show that when the residence time of sediments in the weathering zone exceeds the amount of time required for the complete dissolution of all weatherable minerals, weathering fluxes increase with increasing erosion rate (supply limitation). Once erosion rates increase enough that sediment residence times drop below a threshold (set by dissolution rates), weathering fluxes plateau ("kinetic" limitation). For pyrite, which is a representative sulfide mineral, oxidation rates are orders of magnitude faster than silicate dissolution (Williamson and Rimstidt, 1994). Thus, the threshold erosion rate at which pyrite oxidation plateaus will also be higher than for silicates. Consequently, we expect a range of erosion rates where pyrite oxidation increases with increasing erosion but silicate weathering does not, leading to the preferential oxidation of pyrite. If pyrite contents are sufficient, environments within this range of high erosion rates will be associated with CO_2 release as we observe in the Andes/Amazon study region.

5. Conclusions

Using a suite of dissolved- and solid-phase measurements, we identify an erosional control on the acid budget of chemical weathering in the Kosñipata/Madre de Dios system. Our results are consistent with a growing body of work showing that sulfide mineral oxidation dominates in mountainous systems (Galy and France-Lanord, 1999; Spence and Telmer, 2005; Calmels et al., 2007; Das et al., 2012; Torres et al., 2014). In our Andean catchments, the proportion of weathering driven sulfide mineral oxidation results in CO_2 release. In the foreland floodplain region, weathering acts as a CO_2 sink despite being less sensitive to seasonal changes in runoff (Torres et al., 2015). The interplay between erosion rates and reaction kinetics we invoke to explain the dominance of pyrite oxidation in the Andes should be applicable to a range of potentially trace phases that react more rapidly than silicates (e.g., carbonate minerals). Overall, this work suggests that the relationship between mountain uplift, weathering, and atmospheric pCO_2 is complex due to the involvement of the sulfur cycle.

Acknowledgements

Financial support was provided by NSF EAR-1227192 and NSF EAR-1455352 to A.J. West. M. Torres was supported by USC and C-DEBI fellowships. K. Clark was supported by NSERC and Clarendon Fund Ph.D. scholarships. We thank ACCA Peru, Incaterra, and CREES for field support; A. Robles Caceres, J.A. Gibaja Lopez, J. Huamán Ovalle, R.J. Abarca Martínez, I. Cuba Torres, A. Alfaro-Tapia, D. Oviedo Licona, A. Ccahuana, and J. Farfan Flores for field assistance. Lou Derry and two anonymous reviewers are thanked for their comments on an earlier version of this manuscript.

Appendix A. Supplementary material

Supplementary material related to this article can be found online at http://dx.doi.org/10.1016/j.epsl.2016.06.012.

References

Andreae, M.O., Berresheim, H., Bingemer, H., Jacob, D.J., Lewis, B.L., Li, S.M., Talbot, R.W., 1990. The atmospheric sulfur cycle over the Amazon Basin: 2. Wet season. J. Geophys. Res. 95, 16,813–16,824. http://dx.doi.org/10.1029/JD095iD10p16813.

Balci, N., Shanks, W.C., Mayer, B., Mandernack, K.W., 2007. Oxygen and sulfur isotope systematics of sulfate produced by bacterial and abiotic oxidation of pyrite. Geochim. Cosmochim. Acta 71 (15), 3796–3811. http://dx.doi.org/10.1016/j.gca.2007.04.017.

Berner, E.K., Berner, R.A., 2012. Global Environment: Water, Air, and Geochemical Cycles. Princeton University Press.

Berner, R.A., 1989. Biogeochemical cycles of carbon and sulfur and their effect on atmospheric oxygen over phanerozoic time. Palaeogeogr. Palaeoclimatol. Palaeoecol. 75, 97–122. http://dx.doi.org/10.1016/0921-8181(89)90018-0.

Bickle, M.J., Tipper, E.D., Galy, A., Chapman, H., Harris, N., 2015. On discrimination between carbonate and silicate inputs to Himalayan rivers. Am. J. Sci. 315, 120–166. http://dx.doi.org/10.2475/02.2015.02.

Bouchez, J., von Blanckenburg, F., Schuessler, J.A., 2013. Modeling novel stable isotope ratios in the weathering zone. Am. J. Sci. 313 (4), 267–308. http://dx.doi.org/10.2475/04.2013.01.

Brantley, S.L., Holleran, M.E., Jin, L., Bazilevskaya, E., 2013. Probing deep weathering in the Shale Hills Critical Zone Observatory, Pennsylvania (USA): the hypothesis of nested chemical reaction fronts in the subsurface. Earth Surf. Process. Landf. 38 (11), 1280–1298. http://dx.doi.org/10.1002/esp.3415.

Calmels, D., Gaillardet, J., Brenot, A., France-Lanord, C., 2007. Sustained sulfide oxidation by physical erosion processes in the Mackenzie River basin: climatic perspectives. Geology 35 (11), 1003–1006. http://dx.doi.org/10.1130/G24132A.1.

Carlotto Caillaux, V.S., Rodriguez, G., Fernando, W., Roque, C., Dionicio, J., Chávez, R., 1996. Geología de los cuadrángulos de Urubamba y Calca. Instituto Geológica Nacional, Lima, Peru.

Clark, K.E., Hilton, R.G., West, A.J., Malhi, Y., Gröcke, D.R., Bryant, C.L., Ascough, P.L., Robles Caceres, A., New, M., 2013. New views on "old" carbon in the Amazon River: insight from the source of organic carbon eroded from the Peruvian Andes. Geochem. Geophys. Geosyst. 14 (5), 1644–1659. http://dx.doi.org/10.1002/ggge.20122.

Clark, K.E., Torres, M.A., West, A.J., Hilton, R.G., New, M., Horwath, A.B., Fisher, J.B., Rapp, J.M., Robles Caceres, A., Malhi, Y., 2014. The hydrological regime of a forested tropical Andean catchment. Hydrol. Earth Syst. Sci. 18 (12), 5377–5397. http://dx.doi.org/10.5194/hess-18-5377-2014.

Clark, K.E., 2014. Patterns and drivers of riverine particulate organic carbon transport in an Andean valley. Ph.D. thesis. Geography and the Environment, University of Oxford, UK. 289 p.

Clark, K.E., West, A.J., Hilton, R.G., Asner, G.P., Quesada, C.A., Silman, M.R., Saatchi, S.S., Farfan-Rios, W., Martin, R.E., Horwath, A.B., Halladay, K., New, N., Malhi, Y., 2016. Storm-triggered landslides in the Peruvian Andes and implications for topography, carbon cycles, and biodiversity. Earth Surf. Dyn. 4, 47–70.

Das, A., Chung, C.H., You, C.F., 2012. Disproportionately high rates of sulfide oxidation from mountainous river basins of Taiwan orogeny: sulfur isotope evidence. Geophys. Res. Lett. 39 (12), 1–6. http://dx.doi.org/10.1029/2012GL051549.

Dellinger, M., Gaillardet, J., Bouchez, J., Calmels, D., Louvat, P., Dosseto, A., Gorge, C., Alanoca, L., Maurice, L., 2015. Riverine Li isotope fractionation in the Amazon River basin controlled by the weathering regimes. Geochim. Cosmochim. Acta 164, 71–93. http://dx.doi.org/10.1016/j.gca.2015.04.042.

Detmers, J., Brüchert, V., Habicht, K.S., Kuever, J., 2001. Diversity of sulfur isotope fractionations by sulfate reducing prokaryotes. Appl. Environ. Microbiol. 67 (2), 888–894. http://dx.doi.org/10.1128/AEM.67.2.888-894.2001.

Dosseto, A., Bourdon, B., Gaillardet, J., Maurice-Bourgoin, L., Allègre, C.J., 2006. Weathering and transport of sediments in the Bolivian Andes: time constraints from uranium-series isotopes. Earth Planet. Sci. Lett. 248 (3–4), 759–771.

Gaillardet, J., Dupre, B., Allegre, C., Négrel, P., 1997. Chemical and physical denudation in the Amazon River Basin. Chem. Geol. 142 (3–4), 141–173.

Galy, A., France-Lanord, C., 1999. Weathering processes in the Ganges–Brahmaputra basin and the riverine alkalinity budget. Chem. Geol. 159 (1–4), 31–60.

Gröger, J., Franke, J., Hamer, K., Schulz, H.D., 2009. Quantitative recovery of elemental sulfur and improved selectivity in a chromium-reducible sulfur distillation. Geostand. Geoanal. Res. 33, 17–27. http://dx.doi.org/10.1111/j.1751-908X.2009.00922.x.

Hercod, D.J., Brady, P.V., Gregory, R.T., 1998. Catchment-scale coupling between pyrite oxidation and calcite weathering. Chem. Geol. 151 (1–4), 259–276.

Hindshaw, R.S., Heaton, T.H., Boyd, E.S., Lindsay, M.L., Tipper, E.T., 2016. Influence of glaciation on mechanisms of mineral weathering in two high Arctic catchments. Chem. Geol. 420.

INGEMMET, 2013. GEOCATMIN – geologia integrada por proyectos regionales. Instituto Geológico Minero Metalúrgico.

Jacobson, A.D., Blum, J.D., 2000. Ca/Sr and ^{87}Sr/^{86}Sr geochemistry of disseminated calcite in Himalayan silicate rocks from Nanga Parbat: influence on river-water chemistry. Geology 28 (5), 463–466.

Leleyter, L., Probst, J., 1999. A new sequential extraction procedure for the speciation of particulate trace elements in river sediments. Int. J. Environ. Anal. Chem. 73 (2), 109–128.

Lerman, A., Wu, L., Mackenzie, F.T., 2007. CO_2 and H_2SO_4 consumption in weathering and material transport to the ocean, and their role in the global carbon balance. Mar. Chem. 106 (1–2), 326–350. http://dx.doi.org/10.1016/j.marchem.2006.04.004.

Longinelli, A., Edmond, J., 1983. Isotope geochemistry of the Amazon basin: a reconnaissance. J. Geophys. Res. 88, 3703–3717.

Louterbach, M., Roddaz, M., Bailleul, J., Antoine, P.O., Adnet, S., Kim, J., van Soelen, E., Parra, F., Gérard, J., Calderon, Y., et al., 2014. Evidences for a paleocene marine incursion in southern Amazonia (Madre de Dios sub-Andean zone, Peru). Palaeogeogr. Palaeoclimatol. Palaeoecol. 414, 451–471.

Lu, F.H., Meyers, W.J., Schoonen, M.A.A., 1997. Minor and trace element analyses on gypsum: an experimental study. Chem. Geol. 142, 1–10. http://dx.doi.org/10.1016/S0009-2541(97)00070-3.

Maher, K., Chamberlain, C.P., 2014. Hydrologic regulation of chemical weathering and the geologic carbon cycle. Science 343 (6178), 1502–1504. http://dx.doi.org/10.1126/science.1250770.

Mendívil Echevarría, S., Dávila Manrique, D., 1994. Geología de los cuadrángulos de Cuzco y Livitaca. Instituto Geológica Nacional, Lima, Peru.

Moquet, J.S., Crave, A., Viers, J., Seyler, P., Armijos, E., Bourrel, L., Chavarri, E., Lagane, C., Laraque, A., Casimiro, W.S.L., Pombosa, R., Noriega, L., Vera, A., Guyot, J.L., 2011. Chemical weathering and atmospheric/soil CO_2 uptake in the Andean and Foreland Amazon basins. Chem. Geol. 287 (1–2), 1–26. http://dx.doi.org/10.1016/j.chemgeo.2011.01.005.

Palmer, M., Edmond, J., 1992. Controls over the strontium isotope composition of river water. Geochim. Cosmochim. Acta 56 (5), 2099–2111.

Paris, G., Sessions, A.L., Subhas, A.V., Adkins, J.F., 2013. MC-ICP-MS measurement of δ^{34}S and Δ^{33}S in small amounts of dissolved sulfate. Chem. Geol. 345, 50–61. http://dx.doi.org/10.1016/j.chemgeo.2013.02.022.

Paytan, A., Kastner, M., Campbell, D., Thiemens, M.H., 1998. Sulfur isotopic composition of Cenozoic seawater sulfate. Science 282 (5393), 1459–1462.

Petford, N., Atherton, M., 1996. Na-rich partial melts from newly underplated basaltic crust: the Cordillera Blanca Batholith, Peru. J. Petrol. 37 (6), 1491–1521.

Playà, E., Rosell, L., 2005. The celestite problem in gypsum Sr geochemistry: an evaluation of purifying methods of gypsiferous samples. Chem. Geol. 221, 102–116. http://dx.doi.org/10.1016/j.chemgeo.2005.04.006.

Ponton, C., West, A.J., Feakins, S.J., Galy, V., 2014. Leaf wax biomarkers in transit record river catchment composition. Geophys. Res. Lett. 41 (18), 6420–6427. http://dx.doi.org/10.1002/2014GL061328.

Roddaz, M., Viers, J., Brusset, S., Baby, P., Hérail, G., 2005. Sediment provenances and drainage evolution of the Neogene Amazonian foreland basin. Earth Planet. Sci. Lett. 239 (1), 57–78.

Spence, J., Telmer, K., 2005. The role of sulfur in chemical weathering and atmospheric CO_2 fluxes: evidence from major ions, δ^{13}C DIC, and δ^{34}S SO_4 in rivers of the Canadian Cordillera. Geochim. Cosmochim. Acta 69 (23), 5441–5458. http://dx.doi.org/10.1016/j.gca.2005.07.011.

Stallard, R., Edmond, J., 1981. Geochemistry of the Amazon 1. Precipitation chemistry and the marine contribution to the dissolved load at the time of peak discharge. J. Geophys. Res. 86 (C10), 9844–9858.

Torres, M.A., West, A.J., Li, G., 2014. Sulphide oxidation and carbonate dissolution as a source of CO_2 over geological timescales. Nature 507 (7492), 346–349. http://dx.doi.org/10.1038/nature13030.

Torres, M., West, A.J., Clark, K.E., 2015. Geomorphic regime modulates hydrologic control of chemical weathering in the Andes–Amazon. Geochim. Cosmochim. Acta 166, 105–128. http://dx.doi.org/10.1016/j.gca.2015.06.007.

Turchyn, A.V., Tipper, E.T., Galy, A., Lo, J.K., Bickle, M.J., 2013. Isotope evidence for secondary sulfide precipitation along the Marsyandi River, Nepal, Himalayas. Earth Planet. Sci. Lett. 374, 36–46. http://dx.doi.org/10.1016/j.epsl.2013.04.033.

Vargas Vilchez, L., Hipolito Romero, A., 1998. Geología de los cuadrángulos de Río Pinquén, Pilcopata y Chontachaca. Hojas: 25-t, 26-t y 27-t. Instituto Geológica Nacional, Lima, Peru.

West, A.J., 2012. Thickness of the chemical weathering zone and implications for erosional and climatic drivers of weathering and for carbon-cycle feedbacks. Geology 40 (9), 811–814. http://dx.doi.org/10.1130/G33041.1.

White, A.F., Bullen, T.D., Vivit, D.V., Schulz, M.S., Clow, D.W., 1999. The role of disseminated calcite in the chemical weathering of granitoid rocks. Geochim. Cosmochim. Acta 63 (13), 1939–1953.

Williamson, M., Rimstidt, J., 1994. The kinetics and electrochemical rate-determining step of aqueous pyrite oxidation. Geochim. Cosmochim. Acta 58 (24), 5443–5454.

Yi-Balan, S.A., Amundson, R., Buss, H.L., 2014. Decoupling of sulfur and nitrogen cycling due to biotic processes in a tropical rainforest. Geochim. Cosmochim. Acta 142, 411–428.

Zeebe, R.E., Wolf-Gladrow, D.A., 2001. CO_2 in Seawater: Equilibrium, Kinetics, Isotopes, vol. 65. Gulf Professional Publishing.

Appendix A. Detailed Methods

Appendix A.1. Solid phase geochemical analyses

Samples of river bank sediments and rocks were collected from across the entire study site in order to constrain the elemental and isotopic composition of different lithologic end-members. Sub-samples of the river bank sediments were separated using a riffle splitter and powdered in a ball mill. Rock samples were disaggregated using an agate mortar and pestle before being ground in a ball mill.

Appendix A.1.1. Bulk XRF measurements

To determine the content of non-volatile elements in the river bank sediment samples, the samples were mixed in a 1:2 ratio with lithium metaborate and then doubly fused in graphite crucibles at 1000°C. The twice fused glass beads were then polished and analyzed by X-ray fluorescence spectroscopy (XRF) at Pomona College. A suite of 35 elements were analyzed. Only measurements of Na, Ca, Mg, and Sr concentrations are discussed in this paper. The stream sediment reference material STSD-2 (Environment Canada) was processed and analyzed using the same procedure in order to check for accuracy. For all reported elements, the measured values of STSD-2 agree with certified values within 10%.

Appendix A.1.2. Solid phase sulfur isotope measurements

Sulfide minerals within rock samples from the Kosñipata valley are present as both macroscopic crystals and veins as well as microscopic disseminated crystals. When macroscopic, sulfide minerals were sampled for sulfur isotopic analyses using a diamond-coated steel drill bit and analyzed without any further preparation. When microscopic, the reduced sulfur compounds were converted to H_2S and precipitated as Ag_2S using the chromium reduction method of Gröger et al. (2009). Briefly, the sample powders were mixed with ethanol and concentrated HCl and then reacted with an acidic $Cr^{2+}Cl_2$ solution in a N_2-flushed digestion vessel. During the reaction, the digestion vessels were heated from below with a hotplate. The liberated H_2S gas was passed through a condenser and bubbled through a solution of

$AgNO_3$ and NH_4OH in order to trap S^{2-} as Ag_2S. For each sample, approximately 1 gram of powder was reacted for one hour.

After the reaction was completed, the Ag_2S was separated from the $AgNO_3$ and NH_4OH solution by centrifugation, rinsed three times with de-ionized water (DIW; 18.2 MΩ resistivity), and dried overnight in an oven at 60°C. Sub-samples of both the pyrite and homogenized Ag_2S powders were sent to the University of Arizona Environmental Isotope Lab where the sulfur isotopic composition was measured using an elemental analyzer coupled to a gas-source IRMS (ThermoQuest Finnigan Delta PlusXL). To check the accuracy and reproducibility of the chromium reduction procedure, an in-house pyrite standard was processed during each session and the procedure was replicated for select samples. Overall, calculated yields for the standards were similar (80-90 %; based on mass of recovered Ag_2S) and the isotopic composition of the Ag_2S produced from the pyrite standard was identical, within the analytical uncertainty (0.15 ‰), to the un-processed pyrite. Similarly, variability between replicate sample extractions was similar in magnitude to the analytical uncertainty (± 0.2 ‰).

Appendix A.1.3. Sequential river bank sediment leaches

In order to selectively dissolve carbonate minerals in the river bank sediment samples, a sequential leaching procedure based on the method of Leleyter and Probst (1999) was used. Both ground and un-ground sediment samples were tested, but only the leaches of the un-ground sediment samples were found to selectively dissolve carbonates to a degree that allowed for the determination of their chemistry. For the un-ground samples, 4-6 grams of sediment were separated from the total sample using a riffle splitter and then split into two roughly equal aliquots that were leached separately in 50 mL polypropylene (PP) centrifuge tubes.

During each leaching step, the sediment samples were kept at room temperature and stirred by laying the tubes on a shaking table set to 200 rpm. After each leaching step, the leachate was first separated from the sediments by centrifugation. The supernatant was then decanted and filtered with a 0.2 μm nylon filter. Before the next leaching step, the sediment samples were rinsed three times with DIW.

To remove soluble salts, the sediments were first leached with 10 mL of DIW for 30 minutes. Next, exchangeable elements were removed by leaching the sediments with 10 mL of 1M NH_4Cl for 2 hours. Finally, carbonate minerals were selectively dissolved by leaching the sediments for 5 hours with 10 mL of a 1M acetic acid solution that was set to a pH of $\sim$4.5 by titration with NH_4OH.

After filtration, the acetic acid leachates were evaporated to dryness in PP vials in a clean laboratory and then re-dissolved in 5% HNO_3. The concentrations of Al, Si, Na, Ca, Mg, Sr, and Li in the leachate solutions were determined with an Agilent 4100 microwave plasma atomic emission spectrometer (MP-AES) calibrated using synthetic standards. The results are reported as nanomoles of element leached per gram of sample.

Appendix A.2. Dissolved phase geochemical analyses

Water samples were collected using slightly different methods depending upon the sampling year. For samples collected before 2012, water was collected from the river surface using a clean PP bottle, filtered on site with a 0.2 μm porosity nylon filter, and split into two 60 mL high-density polyethylene bottles (HDPE). One of the 60 mL HDPE bottles was preserved with 2 drops of high purity HCl dispensed from an acid-washed Teflon dropper bottle for cation analyses. The other HDPE bottle was left unpreserved. In the laboratory, samples with any remaining particulates (e.g., from flocculated aggregates forming after field filtration) were re-filtered before analysis with a 0.2 μm nylon porosity filter.

After 2012, water samples were collected from the river surface with a clean PP bucket and transferred to 10 L plastic bags before filtration. Within 24 hours of collection, the samples were filtered with 0.2 μm porosity polyethersulfone (PES) filters housed in a teflon filtration unit with a peristaltic pump and tygon tubing. The filtrate was collected directly into two clean 60 mL HDPE bottles. One of the 60 mL HDPE bottle was preserved with 60 μL of concentrated distilled HNO_3 dispensed from a teflon vial with an acid-washed pipette tip. The other HDPE bottle was left unpreserved.

Appendix A.2.1. Cation and Si concentrations

To determine the concentrations of Na, K, Ca, Mg, Si, Li, and Sr, the acidified water samples were analyzed using an MP-AES calibrated with synthetic standards. Precision and accuracy was assessed by analyzing a reference material every 15 samples. For Ca, Mg, Na, K, and Si, the reference material ION-915 was used (Environment Canada). For Li, the reference material TMDA-51.4 (Environment Canada) was used. For Sr, an in-house prepared $SrCO_3$ solution was used. Replicate analyses of each solution reveals an analytical precision within 5% (1σ) for each analyte.

Appendix A.2.2. Anion concentrations

To determine the concentrations of Cl^- and SO_4^{2-}, the un-acidified samples were analyzed with a Metrohm ion chromatograph equipped with a Metrosep A4/150 column and a conductivity suppressor. The elements were eluted from the column with 3.2 mM Na_2CO_3 and 1.0 mM $NaHCO_3$ at a flow rate of 0.7 mL min^{-1}. The instrument was calibrated using synthetic standards. Precision and accuracy was assessed by analyzing a certified reference material (ION-915, Environment Canada) after every 15 samples. Replicate analyses of ION-915 reveals an analytical precision within 5% (1σ) for each analyte.

Appendix A.2.3. Sulfate-sulfur isotope measurements

To measure the $\delta^{34}S_{V-CDT}$ of dissolved SO_4^{2-}, SO_4^{2-} was purified from $\sim$ 1-10 mL of sample using either a cation or anion exchange resin following established protocols (Paris et al., 2013). Before separation, all samples were evaporated to dryness within a clean laboratory. For samples purified using a cation exchange resin, the sample residue was re-dissolved in 0.25 % HCl and introduced into a column containing Bio-Rad AG50X8 resin following Paris et al. (2013). For sample purified using an anion exchange resin, the sample residue was re-dissolved in 0.5 % HCl and introduced into a column of AG1X8 resin following Paris et al. (2014). After elution from the columns, the samples were evaporated to dryness and then re-dissolved in 5% HNO_3. Before analysis, all samples were diluted and mixed with a sodium solution to match the sodium and sulfate concentrations of the bracketing standard. The samples were then analyzed using a Thermo Neptune Plus multi-collector inductively coupled plasma mass spectrometer (MC-ICP-MS) at Caltech using sample-standard bracketing to correct for instrumental drift and mass bias following Paris et al. (2013).

Replicate purification of sulfate and measurement of its sulfur isotopic composition from select samples reveals variability of up to 0.2 ‰. This uncertainty value is reported in all figures and tables but is not included after each value in the main text for brevity.

Appendix A.2.4. Strontium isotope measurements

To measure the radiogenic ($^{87}Sr/^{86}Sr$) isotopic composition of dissolved Sr, the acidified samples were purified using an automated HPLC separation with Sr Spec resin at the Institute de Physique du Globe Paris (IPGP; Meynadier et al. 2006). The purified samples were evaporated to dryness, re-dissolved in 0.5 M HNO_3 and analyzed on a Thermo Neptune plus MC-ICP-MS at IPGP. A solution made from the NIST carbonate reference material SRM987 was used to check accuracy regularly. To correct for Kr interference, the ^{83}Kr/^{84}Kr and ^{83}Kr/^{86}Kr ratios were determined using the blank solution at the beginning of the run and the ^{83}Kr signal was monitored for each sample and standard. To correct for Rb interference, the ^{87}Rb signal of a 5 ppb Rb solution was measured at the beginning of the run and the ^{85}Rb signal was monitored for each sample and standard.

The individual analytical uncertainty on each of the dissolved ^{87}Sr/^{86}Sr ratio measurements is less then 0.1 permil. Nonetheless, given the large range of variability between samples, the measured ^{87}Sr/^{86}Sr ratios are only be reported to three decimal places in the main text.

Appendix A.3. Inversion Model

The inversion model is based on the mixing equation:

$$X/\Sigma^{+}_{measured} = \sum_{f=1}^{n} F_f \times X/\Sigma^{+}_{f} \tag{A.1}$$

where $X/\Sigma^+_{measured}$ is a measured elemental ratio of element X, F_f is the fractional contribution of end-member f, X/Σ^+_f is the elemental ratio of end-member f, and n is the number of end-members. For isotopic ratios, we use the modified mixing equation:

$$\delta X_{measured} \times X/\Sigma^+_{measured} = \sum_{f=1}^{n} F_f \times X/\Sigma^+_f \times \delta X_f \tag{A.2}$$

where $\delta X_{measured}$ is the measured isotopic ratio of element X and δX_f is the isotopic ratio of end-member f.

To perform the inversion, a single value for each end-member ratio (X/Σ^+_f and δX_f) is randomly drawn from a predefined uniform distribution (see Table 1). Then, using these random end-member values and the measured ratios ($X/\Sigma^+_{measured}$ and $\delta X_{measured}$), the fractional contribution from each end-member (F_f) is calculated using the mldivide command in MATLAB 2015b. For each sample, we repeat this approach 6×10^4 times in order to ensure that a sufficient number of random end-member combinations are used so that the reported confidence intervals do not change appreciably between replicate calculations. If any of the calculated mixing fractions are negative, the results of that simulation are discarded. While this general approach applies to all of the mixing models, details specific to the different versions described in the main text are included below. The precise end-member definitions are included in Table 1.

Appendix A.3.1. Na-Ca-Mg-Cl-SO_4-$\delta^{34}S$ inversion

To apportion the solute budget between limestone, dolomite, granite, shale, rainfall, and evaporites, we use Cl/Σ^+, Na/Σ^+, Ca/Σ^+, Mg/Σ^+, SO_4/Σ^+, and $\delta^{34}S$. With the added constraint that the fractional contributions from each end-member must all sum to one, this model includes 7 equations, which is one greater than the number required for 6 end-members. Consequently, we calculate a least squares solution for each simulation. Since some of the simulations calculated this way will have large errors, we calculate the sum of the squared residuals (SSE) for each simulation. For each sample, we calculate a reference SSE by determining the 5^{th} percentile value of SSE for all of the simulations for that sample. We then select only the subset of simulations where the SSE is less than this reference value. Together, all of the constraints result in an average of 224 valid simulations for each sample. For this model, the *a posteriori* values of SO_4/Σ^+ for the carbonate and silicate end-members are used to determine the proportions of sulfuric acid weathering for each sample. For reference, the exact mixing model is included as a MATLAB script (`Torres_etal_A_inversion.m`).

Appendix A.3.2. Na-Ca-Mg-Cl inversion

To apportion the solute budget between limestone, dolomite, granite, shale, and rainfall, we use Cl/Σ^+, Na/Σ^+, Ca/Σ^+, and Mg/Σ^+. With the added constraint that the fractional contributions from each end-member must all sum to one, this model includes 5 equations. Since the system is not over-constrained, we calculate an exact solution for each combination of random end-members. Together, all of the constraints result in an average of 4649 valid simulations for each sample. For reference, the exact mixing model is included as a MATLAB script (`Torres_etal_B_inversion.m`).

Appendix A.4. Sr isotope model

For each simulation that produces a set of realistic mixing proportions, the predicted Sr/Σ^+ and $^{87}Sr/^{86}Sr$ are calculated using equations A.1 and A.2. This calculation is repeated 1000 times using different end-member values for Sr/Σ^+ and $^{87}Sr/^{86}Sr$. Combinations of end-members and mixing fractions that produce values of Sr/Σ^+ that are more than 5% from the measured values are discarded. For reference, the exact mixing model is included as a MATLAB script (`Torres_etal_C_inversion.m`).

Appendix A.4.1. Li/Σ^+ model

For each calculation that produces a set of realistic mixing proportions, the Li/Σ^+ of the sample is calculated using equation A.1. Only shale and granite are considered as Li sources. To get Li/Σ^+ values for these end-members, we multiply the Li/Na ratios from Dellinger et al. (2015) by the end-member Na/Σ^+ used in the simulation. For reference, the exact mixing model is included as a MATLAB script (`Torres_etal_D_inversion.m`).

Appendix A.5. Effect of weathering on pCO_2

The fluxes of alkalinity and DIC delivered to the ocean by chemical weathering depend upon the relative magnitude of different weathering reactions. Here, we consider how the proportion of cations sourced from carbonate weathering and the proportion of total weathering driven by sulfuric acid set the relative amounts of alkalinity and DIC production. By defining reference ratios of alkalinity to DIC that are associated with no change in pCO_2, we determine which combinations of weathering reactions increase or decrease atmospheric pCO_2 over different timescales.

Appendix A.5.1. Relevant Chemical Reactions

To quantify the effects of different weathering reactions on the budgets of alkalinity and DIC, we start by writing the acid consuming (carbonate and silicate dissolution) and acid producing (carbonic acid disassociation and pyrite oxidation) half-reactions. We then combine these half reactions in order to write full reactions for the weathering of carbonate and silicate minerals by carbonic and sulfuric acids. Finally, by comparing the relative amounts of DIC and alkalinity production resulting from each reaction, we determine how the proportion of cations sourced from carbonate weathering and the proportion of total weathering driven by sulfuric acid set the effect of weathering on atmospheric pCO_2 over different timescales.

The half-reactions for the proton-promoted dissolution of carbonate and silicate minerals can be written as:

$$2H^+ + CaCO_3 \leftrightarrow Ca^{2+} + H_2CO_3 \tag{A.3}$$

and

$$4H^+ + Ca_2SiO_4 \leftrightarrow H_4SiO_4 + 2Ca^{2+} \tag{A.4}$$

The corresponding half-reactions for acid generation by the disassociation of carbonic acid and the oxidation of pyrite can be written as:

$$H_2CO_3 \leftrightarrow 2H^+ + CO_3^{2-} \tag{A.5}$$

and

$$4FeS_2 + 15O_2 + 14H_2O \leftrightarrow 8SO_4^{2-} + 16H^+ + 4Fe(OH)_3 \tag{A.6}$$

The acid consuming half reactions (carbonate and silicate dissolution) can be combined with the acid generating half reactions (carbonic acid disassociation and pyrite oxidation) to generate full reactions describing the weathering of carbonate and silicate minerals by carbonic and sulfuric acid. To do this, we combine the above equations with the assumption that the number of moles of protons generated and consumed should be equal. We also follow the convention of writing all species as the dominant species at the carbonic acid equivalence point. In particular, this means that we will write all DIC species as $\mathrm{H_2CO_3}$ and balance reactions by adding $\mathrm{H^+}$ ions as needed. The utility of this approach is that, after canceling out species that appear on both sides of an equation, any $\mathrm{H_2CO_3}$ species that appear on the right hand side of an equation reflect DIC generation and any $\mathrm{H^+}$ species that appear on the left hand side of an equation reflect alkalinity production. This approach yields the full equations:

$$2H^+ + CaCO_3 \leftrightarrow Ca^{2+} + H_2CO_3 \tag{A.7}$$

$$0.5FeS_2 + \frac{15}{8}O_2 + \frac{7}{4}H_2O + CaCO_3 \leftrightarrow Ca^{2+} + H_2CO_3 + SO_4^{2-} + 0.5Fe(OH)_3 \tag{A.8}$$

$$4H^+ + Ca_2SiO_4 \leftrightarrow H_4SiO_4 + 2Ca^{2+} \tag{A.9}$$

and

$$FeS_2 + \frac{15}{4}O_2 + \frac{7}{2}H_2O + Ca_2SiO_4 \leftrightarrow H_4SiO_4 + 2Ca^{2+} + 2SO_4^{2-} + Fe(OH)_3 \tag{A.10}$$

for carbonate-carbonic, carbonate-sulfuric, silicate-carbonic, and silicate-sulfuric weathering respectively.

To compare their effects on DIC and alkalinity, we normalize all of the full weathering reactions (equations A.7 - A.10) by the charge equivalents of cations released, which is the quantity shown in Table A.1. This normalization insures that the results are not sensitive to the chosen mineral formula. This is particularly important for silicate minerals, which typically contain cations other than Ca^{2+} in appreciable amounts. This normalization also aids in the assessment of field data since estimates of chemical weathering in rivers are based on measurements of cation release.

Using the coefficients in Table A.1, we can write equations for the production of alkalinity and DIC by weathering where

$$Alkalinity = (z \times (0x + 0y)) + ((1 - z) \times (x + y) \tag{A.11}$$

and

$$DIC = (z \times (0.5x + 0y)) + ((1 - z) \times (0.5x + 0y) \tag{A.12}$$

with z being the proportion of weathering driven by sulfuric acid, x being the charge equivalents of cations contributed by carbonate weathering, and y being the charge equivalents of cations contributed by silicate weathering.

Appendix A.5.2. Short Timescales

In the modern ocean, the ratio of alkalinity to DIC is approximately one. Consequently, on timescales shorter than the timescale associated with marine carbonate burial, atmospheric pCO_2 will increase if the ratio of alkalinity to DIC delivered by rivers is less than

Table A.1: Alkalinity and DIC contributions per unit cation released (charge equivalents) for different weathering reactions

Mineral/Acid	**ΔAlk**	**ΔDIC**
Carbonate-Carbonic	1	0.5
Carbonate-Sulfuric	0	0.5
Silicate-Carbonic	1	0
Silicate-Sulfuric	0	0

1. We note that this is strictly valid for the modern oceanic alkalinity to DIC ratio. To graphically show the implied effects of different combinations of weathering reactions on atmospheric pCO_2, we set equations A.11 and A.12 both equal to one in order to solve for parameter combinations that yield no change in atmospheric pCO_2 on short timescales, which gives the relationship

$$z_{short} = 1 - (0.5 \times R) \tag{A.13}$$

where R is the proportion of cations sourced from carbonate weathering, i.e.:

$$R = \frac{x}{x+y} \tag{A.14}$$

In a plot of R versus z (Figure 7), data that plot above the line described by Equation A.13 are associated with CO_2 release on timescales shorter than carbonate precipitation assuming close to modern conditions.

Appendix A.5.3. Long Timescales

Carbonate burial exports alkalinity and DIC from the ocean in a 2 to 1 ratio (reverse of equation A.7). So, on timescales longer than carbonate burial but shorter than pyrite burial ($< 10^7$ years; Berner and Berner 2012), atmospheric pCO_2 will increase if rivers deliver alkalinity and DIC to the ocean in a ratio that is less than 2. We suggest that this reference alkalinity to DIC ratio should be valid regardless of the oceanic alkalinity to DIC ratio. To graphically show the implied effects of different combinations of weathering reactions on atmospheric pCO_2 over long timescales, Equations A.11 and A.12 can be solved for when

Alk/DIC is equal to two, which gives the equation:

$$z_{long} = 1 - R \tag{A.15}$$

In a plot of R versus z (Figure 7), data that plot above the line described by Equation A.15 are associated with pCO_2 increase on timescales longer than carbonate precipitation but shorter than pyrite burial.

References

Berner, E.K., and Berner, R.A., 2012, Global environment: water, air, and geochemical cycles: Princeton University Press.

Dellinger, M., Gaillardet, J., Bouchez, J., Calmels, D., Louvat, P., Dosseto, A., Gorge, C., Alanoca, L., and Maurice, L., 2015, Riverine Li isotope fractionation in the Amazon River basin controlled by the weathering regimes: Geochimica et Cosmochimica Acta, doi:10.1016/j.gca.2015.04.042.

Gröger, J., Franke, J., Hamer, K., and Schulz, H.D., 2009, Quantitative recovery of elemental sulfur and improved selectivity in a chromium-reducible sulfur distillation: Geostandards and Geoanalytical Research, v. 33, p. 17–27, doi:10.1111/j.1751-908X.2009.00922.x.

Leleyter, L., and Probst, J., 1999, A new sequential extraction procedure for the speciation of particulate trace elements in river sediments: International Journal of Environmental Analytical Chemistry, v. 73, no. 2, p. 109–128.

Meynadier, L., Gorge, C., Birck, J.L., and Allègre, C.J., 2006, Automated separation of Sr from natural water samples or carbonate rocks by high performance ion chromatography: Chemical Geology, v. 227, no. 1-2, p. 26–36, doi:10.1016/j.chemgeo.2005.05.012.

Paris, G., Adkins, J.F., Sessions, A.L., Webb, S.M., and Fischer, W.W., 2014, Neoarchean carbonate-associated sulfate records positive 33S anomalies: Science, v. 346, no. 6210, p. 739–742.

Paris, G., Sessions, A.L., Subhas, A.V., and Adkins, J.F., 2013, MC-ICP-MS measurement of δ^{34}S and Δ^{33}S in small amounts of dissolved sulfate: Chemical Geology, v. 345, p. 50–61, doi:10.1016/j.chemgeo.2013.02.022.